JMES The International Journal of
Mechanical Engineering and Sciences
https://iptek.its.ac.id/index.php/jmes
e-ISSN 2580-7471

Aerodynamic Performance Analysis of Tandem Savonius Wind Turbines Influenced by Lateral Gap from Adjacent Wall

Audha Fitrah Aulina[1*], Haning Hasbiyati[2]

[1]Automotive Engineering Department, Politeknik Negeri Jember, Jember 68121 Indonesia
[2]Renewable Energy Engineering Department, Politeknik Negeri Jember, Jember 68121, Indonesia

Received: 30 Agustus 2025, Revised: 30 September 2025, Accepted: 26 February 2026

Abstract

This research investigates the performance of the Savonius wind turbine through a two-dimensional Computational Fluid Dynamics (CFD) analysis, employing the realizable $k-\varepsilon$ turbulence model with enhanced wall treatment. The primary objective is to examine how variations in the gap-to-diameter ratio $(\mathrm{G/D})$—defined as the distance between the centers of the turbines relative to the blade diameter—affect the aerodynamic behavior and performance of a tandem Savonius wind turbine configuration. In this study, three $\mathrm{G/D}$ ratios are analyzed, namely 1.75, 2, and 2.25, under a uniform freestream wind velocity of $7\ \mathrm{m/s}$. The simulation results indicate that flow deflection between the turbines induces opposite rotational directions: the fore turbine rotates counterclockwise, while the rear turbine rotates clockwise, particularly at higher tip speed ratios. Performance analysis reveals that the fore turbine achieves its maximum efficiency at a $\mathrm{G/D}$ ratio of 2, whereas the rear turbine performs optimally at a $\mathrm{G/D}$ ratio of 1.75.

Keywords: Savonius Wind Turbine, Tandem Configuration, Adjacent Wall

1. Introduction

The Paris Agreement (2015) aims to limit global temperature rise to below $2°\mathrm{C}$ to mitigate the impacts of climate change [1]. Indonesia has updated its Nationally Determined Contributions (NDCs) four times since 2015, with the Enhanced NDC (2022) targeting a 31.89% emissions reduction through domestic efforts and 43.2% with international collaboration by 2030 [2]. To achieve these goals, Indonesia is prioritizing renewable energy sources, including wind power. The National Institute of Aeronautics and Space of Indonesia (*Lembaga Penerbangan dan Antariksa Nasional*, LAPAN) reported that several regions—including East Nusa Tenggara, West Nusa Tenggara, South Sulawesi, and southern Java—have wind velocity exceeding 5 m/s, providing an onshore wind energy potential of 60.6 GW [3].

Wind turbines are critical components in wind power generation. Turbines are classified as vertical-axis (VAWT) or horizontal-axis (HAWT) types depending on the wind direction relative to the rotor axis. The Savonius turbine, a drag-type VAWT, features S-shaped blades—advancing blades (concave profile, capturing wind) and returning blades (convex profile). While Savonius turbines offer low start-up speed capabilities, they typically suffer from low efficiency.

Tandem configurations have been reported to improve turbine performance. For example, Helical Savonius Hydrokinetic Turbines (HSHKT) achieve optimal performance at $\mathrm{L} = 4\mathrm{D}$ spacing [4]. Increasing turbine spacing reduces vortex interactions, improving the first rotor's power production while reducing velocity at the second rotor due to channel wall friction. Similar findings were reported by [5], who noted that closer spacing degrades performance due to stronger rotor interactions, while wider spacing enhances it. A study involving four tandem Savonius turbines showed performance degradation at short distances due to wake interactions, while spacing up to $\mathrm{T/D} = 60$ reduced interference [6]. At close distances, interactions between turbines become stronger and results in a decrease in performance in all turbines. Increasing the distance to $\mathrm{T/D} = 60$, the influence of disturbances from turbine 3 and 4 is reduced which results in turbines 1 and 2 producing performance similar to a single turbine. However, turbines 3 and 4 are still affected by wake region caused by turbines 1 and 2 and causes low performance. In addition, the increasing distance between turbine causes an increase in performance in all turbines because the turbines do not affect each other.

Turbine placement relative to nearby structures also affects performance. Savonius turbines positioned near cross-sectional buildings showed power generation improvements of 208.72% and 439.95% at optimal angles of $60°$ and $90°$ [7]. Similarly, turbines integrated within building tunnels achieved a 62% performance increase

*Corresponding author. Email: audha_fitrah@polije.ac.id, phone: +62 889 0195 4165

at $x/L = 0.5$ and $w/W = 1/9$ [8]. Then, the location of the tunnel also has an effect, (The location of the tunnel also has an effect,) where the best configuration is obtained at vertical location $(f/H) = 0.9$ and lateral location $(S/W) = 0.665$ with a maximum power coefficient obtained of 0.349 (maximum power coefficient of 0.349) at TSR = 1. Placement above forward-facing steps enhanced low-pressure regions and torque production [9]. The introduction of a step has been shown to generate a larger low-pressure region compared to a flat surface, while simultaneously reducing the extent of the high-pressure region on the convex side of the returning blade. This phenomenon contributes to an increased pressure differential, which in turn enhances the torque output of the Savonius wind turbine.

Previous studies have reported that both the tandem configuration and the relative positioning of Savonius wind turbines exert a significant influence on overall performance. Nevertheless, despite the extensive studies that have been conducted previously, there has been no investigation addressing the combined influence of wall distance on Savonius wind turbines arranged in a tandem configuration, particularly under the condition where the advancing blade of the fore turbine is placed near the returning blade of the rear turbine. Accordingly, the present study aims to examine the effect of the gap-to-diameter ratio (G/D) between turbine centers on the performance of tandem Savonius wind turbines. Investigations were conducted using G/D ratios of 1.75, 2.0, and 2.25 under a uniform wind velocity of 7 m/s. The lateral gap acts as a flow modifier that directs and accelerates the incoming wind toward the rotor blades, generating nozzle and blockage effects that strongly influence the torque production. A narrower gap tends to increase local acceleration and pressure gradients, while a wider gap reduces these interactions but diminishes the wall confinement effect. Therefore, the lateral gap becomes a crucial parameter in determining whether the wall effect improves or degrades turbine performance.

2. Method

2.1. Computational Domain and Boundary Conditions

This study employs a two-dimensional modeling approach to analyze the flow around the Savonius wind turbine. The computational model is divided into two domains: a rotating domain and a stationary domain, as illustrated in Figure 1(a). The rotating domain encompasses the Savonius rotor, which rotates throughout the simulation process. In contrast, the stationary domain, which remains fixed during the simulation, includes the inlet, wall, and outlet boundaries. The type and dimensions of the stationary domain were adopted in accordance with the methodologies described in [10] and [11].

Boundary conditions were prescribed to ensure numerical stability and accurately represent the physical flow field within the computational domain. In this study, the boundaries consist of the inlet, outlet, walls, and the Savonius turbine blades, distributed across both the rotating and stationary domains. At the inlet, a uniform wind velocity of 7 m/s was specified, with a turbulence intensity of 2.3% and a turbulent length scale of 66 mm to characterize the upstream flow conditions. A pressure outlet boundary condition with a gauge pressure of 0 Pa was imposed at the outlet to allow for fully developed flow. All stationary walls were modeled with a no-slip condition to capture viscous effects. The Savonius turbine blades were defined as moving walls with prescribed rotational motion, also subject to a no-slip condition, following the methodology reported in [12]. A schematic representation of the applied boundary conditions is shown in 1(a).

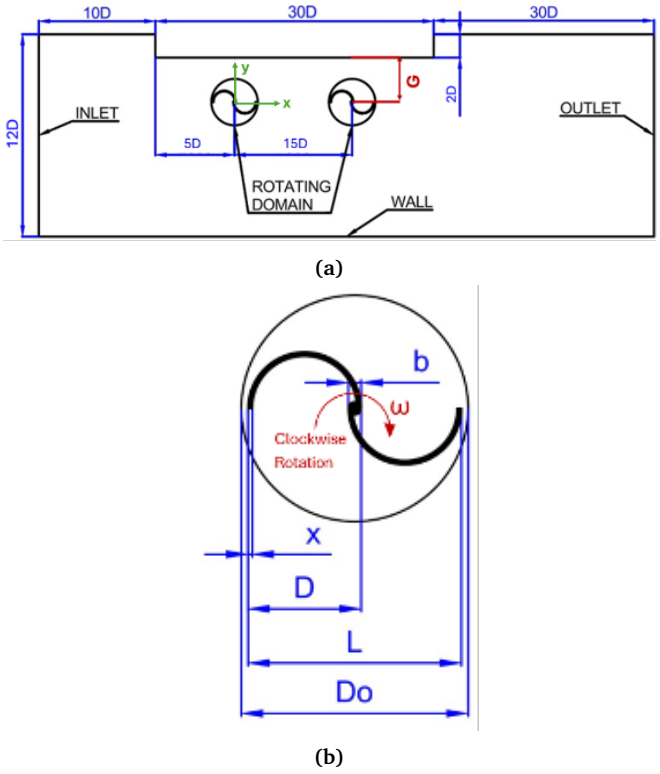

Figure 1. Computational domain and boundary condition (a) All domain; (b) Savonius Turbine.

Table 1. Savonius wind turbine specification for this study.

Savonius Wind Turbine Specification	
Blade diameter (D)	500 mm
Turbine diameter (L)	940 mm
Shaft diameter (b)	60 mm
Endplate diameter (D_0)	1000 mm
Blade thickness (x)	25 mm

This study utilizes a Savonius wind turbine with a blade diameter (D) of 500 mm and a characteristic length (L) of 940 mm. The rotor rotation is oriented clockwise.

The turbine's detailed specifications are provided in Table 1, while its geometric configuration is illustrated in Figure 1(b). In this study, the endplate (D_0) serves as an interface that separates the rotating domain from the stationary domain.

2.2. Meshing

The geometry was discretized into finite elements to facilitate numerical computations, as shown in the mesh configuration in Figure 3. A structured mesh was applied to the stationary domain through systematic subdivision using guidelines, while an unstructured mesh with inflation layers was employed in the rotating domain to capture boundary-layer flow features accurately. The generated mesh satisfies recommended quality metrics, with a maximum skewness of less than 0.95 and a minimum orthogonal quality exceeding 0.1, thereby ensuring both numerical stability and solution fidelity [13].

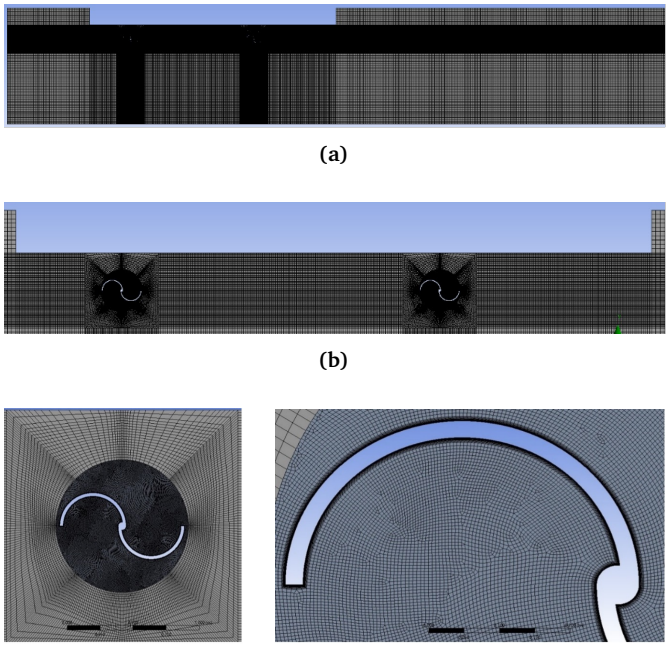

(a) **(b)** **(c)** **(d)**

Figure 3. Meshing results (a) All domain; (b) Wall and turbines; (c) Turbine; and (d) Blade.

2.3. Numerical Models

The fluid flow surrounding the turbine is turbulent in nature, characterized by a high Reynolds number. To achieve accurate computational results, a turbulence model must be employed to describe the complex flow behavior. The $k-\varepsilon$ turbulence model addresses this requirement by solving transport equations for the turbulent kinetic energy (k) and the energy dissipation rate (ε). In ANSYS, three formulations of the $k-\varepsilon$ model are available: Standard, RNG, and Realizable. The Realizable $k-\varepsilon$ model not only satisfies fundamental Reynolds number constraints but also yields improved predictions of spreading rates in jet and nozzle flows, while providing reliable performance in vortical, separated, and recirculating flows as well as in boundary layers subjected to strong pressure gradients. The governing equations of the Realizable $k-\varepsilon$ model are expressed in Equations (1) and (2).

$$\frac{\partial}{\partial t}(\rho k)+\nabla\cdot(\rho\mathbf{u}k)=\nabla\cdot\left[\rho\left(\nu_l+\frac{\nu_t}{\sigma_{t,k}}\right)\nabla k\right]+\rho(P_k-\varepsilon) \tag{1}$$

$$\frac{\partial}{\partial t}(\rho\varepsilon)+\nabla\cdot(\rho\mathbf{u}\varepsilon)=\nabla\cdot\left[\rho\left(\nu_l+\frac{\nu_t}{\sigma_{t,\varepsilon}}\right)\nabla\varepsilon\right]+\rho\left(\frac{C_{1\varepsilon}S\varepsilon-C_{2\varepsilon}\varepsilon^2}{k+\sqrt{\nu_l\varepsilon}}\right) \tag{2}$$

where

$$C_1=\max\left[0.43\frac{\eta}{\eta+5}\right]$$

$$\eta=S\frac{k}{\varepsilon}$$

$$S=\sqrt{2S_{ij}S_{ij}}$$

$$S_{ij}=\frac{1}{2}\left(\frac{\partial u_j}{\partial x_i}+\frac{\partial u_i}{\partial x_j}\right)$$

Other parameters utilized in this investigation are $C_{1\varepsilon}=1.44$, $C_{2\varepsilon}=1.9$, $\sigma=1.0$, and $\sigma=1.2$.

In this study, the Realizable $k-\varepsilon$ model with enhanced wall treatment was adopted for the numerical analysis, given its improved capability to predict complex flow behavior relative to alternative $k-\varepsilon$ turbulence models [14]. Within the cell zone condition settings, the rotating domain was defined using mesh motion [15], with the rotational speed adjusted according to the turbine operating conditions. The tip speed ratio (TSR) and the incoming flow velocity determine the rotor's angular velocity. Furthermore, the rotor speed significantly influences the selection of the time step size (TSS) used in the numerical simulations. The TSS values applied in this study are summarized in Table 2. The equations used to calculate the tip speed ratio (TSR), moment coefficient (C_m), power coefficient (C_p), and time step size (TSS) are expressed as follows:

$$\text{TSR}=\frac{\omega\cdot R}{V} \tag{3}$$

$$C_m=\frac{T}{\frac{1}{2}\cdot\rho\cdot A\cdot R\cdot V^2} \tag{4}$$

$$\text{CoP}=C_m\cdot\text{TSR} \tag{5}$$

$$\text{TSS}=\frac{60}{N}\times\frac{\theta}{360} \tag{6}$$

where ω is the angular velocity, V is the flow velocity, θ is

Table 2. Time step size.

TSR	V (m/s)	ω (rad/s)	Time Step Size
0.2	7	2.979	0.005856
0.4	7	5.957	0.002928
0.6	7	8.936	0.001952
0.8	7	11.915	0.001464
1.0	7	14.894	0.001171
1.2	7	17.872	0.000976
1.4	7	20.851	0.000837
1.6	7	23.830	0.000732
1.8	7	26.809	0.000651
2.0	7	29.787	0.000586
2.2	7	32.766	0.000532

the azimuth angle, N is the rotational speed of the turbine (rpm), and R is the turbine diameter, expressed by the following equation:

$$R = 2D - \frac{b}{2} \tag{7}$$

2.4. Grid Independence Test

The accuracy of numerical results is influenced by the number of mesh elements. To assess this effect, a grid independence test (GIT) was performed by varying mesh density under identical solver settings. The appropriate mesh size was determined at the point where the solution became stable.

Table 3. Grid independence test results.

Elements	Tip Speed Ratio	Moment Coefficient	Error (%)
56739	1	0.08620	—
74639	1	0.07385	16.72333
112179	1	0.07193	2.663875
129655	1	0.07163	0.42518
164187	1	0.07157	0.08156

For this study, the GIT was applied to a conventional rotor [16] using meshes ranging from 56,000 to 164,000 elements at a tip speed ratio of 1. As shown in Table 3 and Figure 4, a mesh size of 110,000 elements produced a moment coefficient within 5% error. Additional refinement beyond this resolution resulted in no meaningful variation. Figure 5 further verifies this outcome, as the moment coefficient versus azimuth angle plots align closely at 110,000 elements. Based on these findings, 110,000 elements were adopted to balance computational cost and accuracy.

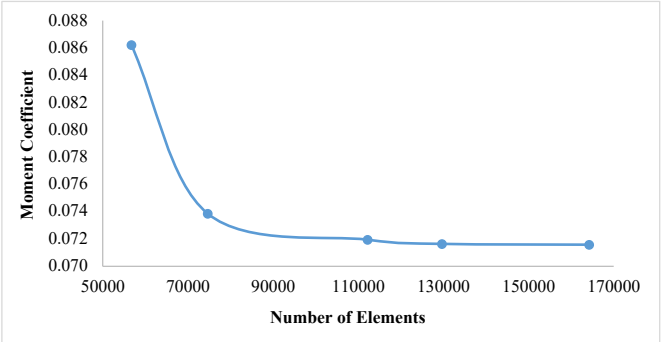

Figure 4. Moment coefficient graph based on the number of mesh elements.

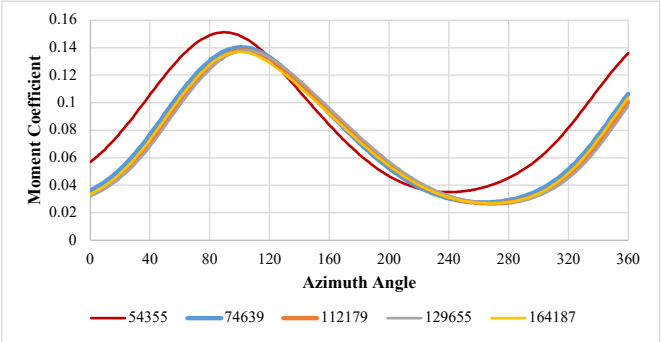

Figure 5. Moment coefficient-azimuth angle curve angle.

2.5. Validation

Model validation was conducted to verify the accuracy of the numerical setup by comparing the present results with reference data. The validation was performed for a single-turbine configuration at a Reynolds number of 140,000, consistent with the conditions in [17]. The moment coefficient data from [17] were used as a benchmark to assess solver accuracy.

As presented in Figure 6 and Table 4, across a TSR range of 0.4-1.2, the deviation between current results and reference data is less than 5%, confirming that the numerical model and solver configuration are appropriately validated.

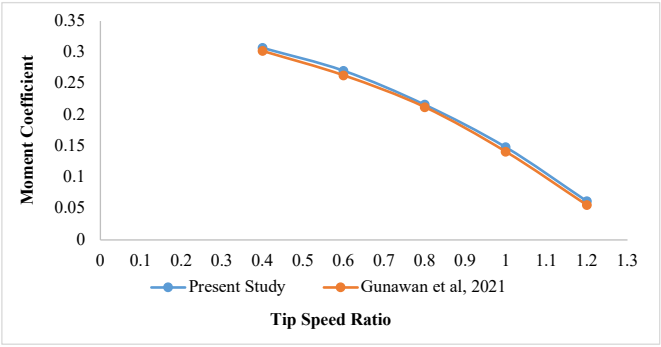

Figure 6. Moment coefficient curve from the validation process.

Table 4. Validation results.

Tip Speed Ratio	Moment Coefficient		Error (%)
	Current Study	Sakti et al (2021)	
0.4	0.306843	0.30185	0.499266
0.6	0.270297	0.26296	0.733747
0.8	0.216023	0.21221	0.381252
1.0	0.148176	0.14095	0.722632
1.2	0.061966	0.05556	0.640568

3. Result and Discussion

3.1. Flow Field Characteristics of the Fore Turbine

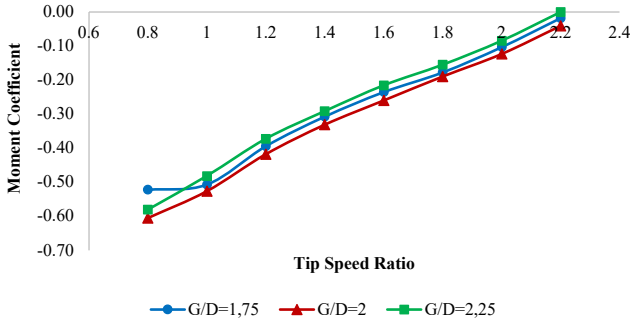

Figure 7. Graph of the moment coefficient for the fore turbine under all configurations.

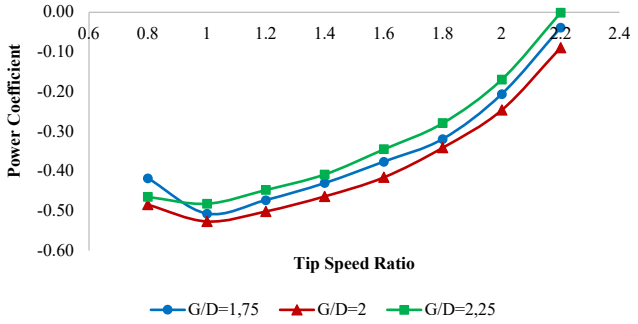

Figure 8. Graph of the power coefficient for the fore turbine under all configurations.

Figure 7 shows the moment coefficient distribution, while Figure 8 illustrates the power coefficient of the fore turbine across all configurations. The differences in these coefficients are relatively small due to the modest variation in G/D ratios. At low tip speed ratios $(\mathrm{TSR} < 1)$, the $\mathrm{G/D} = 1.75$ configuration records the lowest moment and power coefficients among the three cases. At higher tip speed ratios $(\mathrm{TSR} \geq 1)$, the lowest values are observed in the $\mathrm{G/D} = 2.25$ configuration, reflecting the reduced influence of the wall as spacing increases. This phenomenon arises because wall-induced flow confinement weakens as the G/D ratio increases. Consequently, the fore turbine demonstrates optimal performance at $\mathrm{G/D} = 2$, where the interaction between the wall and rotor produces the highest moment and power coefficients while enabling efficient operation at relatively high rotational speeds. This suggests that moderate spacing ratios $(\mathrm{G/D} \approx 2)$ provide the most favorable balance between wall effects and aerodynamic efficiency.

Table 5 presents the velocity contours of the fore turbine for all configurations at an azimuth angle of $90°$. Increasing the gap between the turbine center and the wall leads to higher flow velocities near the tip of the advancing blade, which enhances turbine performance. However, this also causes the moment coefficient for $\mathrm{G/D} = 2.25$ at low tip speed ratios to become more negative, indicating counter clockwise rotor rotation.

At a tip speed ratio of 1, a vortex is observed forming near the convex side of the advancing blade as the gap increases. This phenomenon confirms that for the $\mathrm{G/D} = 2.25$ configuration, both the moment coefficient and power coefficient decrease at higher tip speed ratios.

The pressure distribution of the fore turbine at an azimuth angle of $90°$ for all configurations is presented in Table 6. The wall placement creates a high pressure zone ahead of the concave side of the advancing blade, indicating that this blade section operates under reduced local flow velocity due to wall-induced deflection. Conversely, portions of the convex side of the returning blade exhibit low-pressure regions, signifying higher local flow velocity. Across all tandem configurations, these low-pressure regions are less pronounced, causing the fore turbine in tandem setups to rotate in a counterclockwise direction.

The lowest pressure region is observed at the tip of the advancing blade, indicating the presence of a nozzle effect within the gap. This nozzle effect significantly influences the turbine's performance. As the tip speed ratio (TSR) increases, the nozzle effect intensifies, leading to a blockage effect that degrades turbine performance. The optimal configuration identified in this study is $\mathrm{G/D} = 2$, where wall placement provides a beneficial influence on turbine operation. However, at $\mathrm{G/D} = 2.25$, turbine performance deteriorates as the influence of the wall weakens, reducing the effectiveness of flow acceleration near the blades.

Table 5. Velocity contours of the fore turbine across all configurations at an azimuth angle of $90°$.

	Tip Speed Ratio		
	0.6	**1**	**1.4**
G/D = 1.75	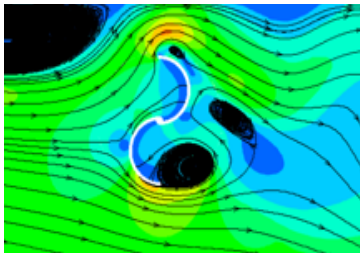	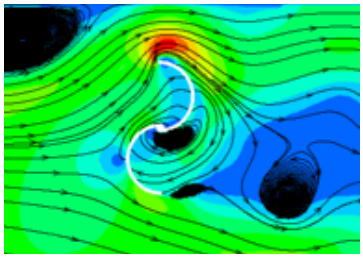	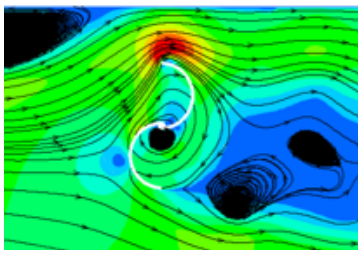
G/D = 2.0	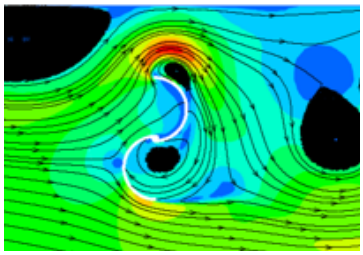	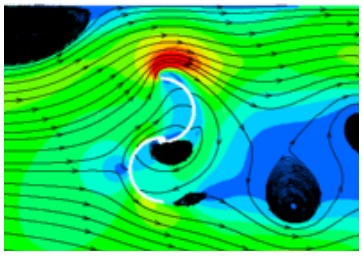	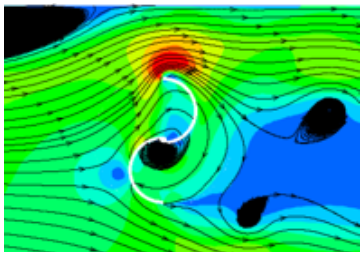
G/D = 2.25	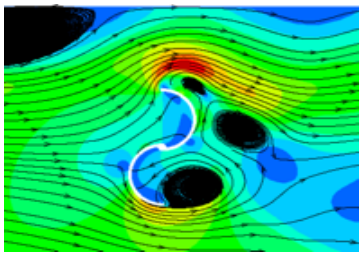	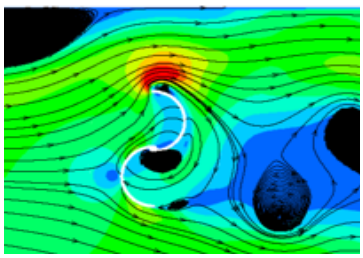	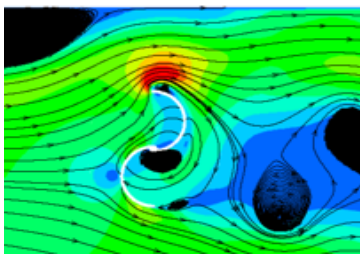

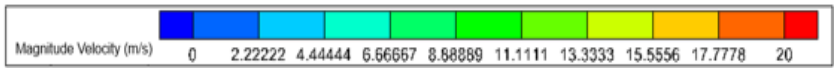

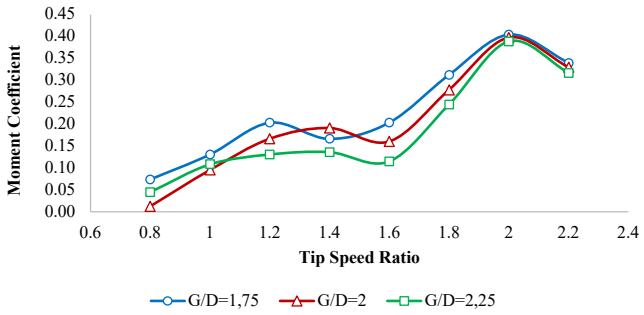

Figure 9. Graph of the moment coefficient for the rear turbine under all configurations.

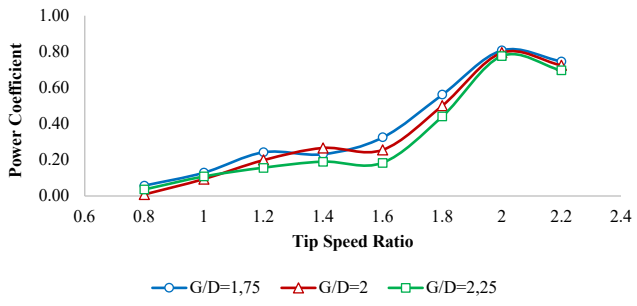

Figure 10. Graph of the power coefficient for the rear turbine under all configurations.

3.2. Flow Field Characteristics of the Rear Turbine

Figure 9 and Figure 10 present the moment coefficient and power coefficient graphs for all configurations. Across all configurations, the rear turbine exhibits both negative and positive values of moment and power coefficients. Negative values indicate that the rear turbine rotates in the counter-clockwise direction, while positive values correspond to clockwise rotation. The occurrence of negative values is attributed to the rear turbine operating within the wake region generated by the fore turbine.

The range of tip speed ratios (TSR) that result in negative values varies with increasing distance gaps. The configuration with $\mathrm{G/D} = 1.75$ produces a negative power coefficient over the narrowest TSR range $(\mathrm{TSR} \leq 0.4)$,

Table 6. Pressure contours of the fore turbine across all configurations at an azimuth angle of 90°.

	Tip Speed Ratio		
	0.6	**1**	**1.4**
G/D = 1.75	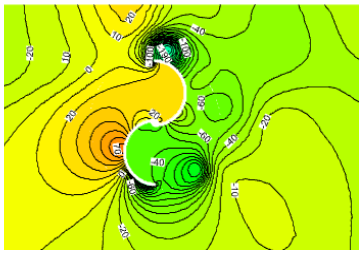	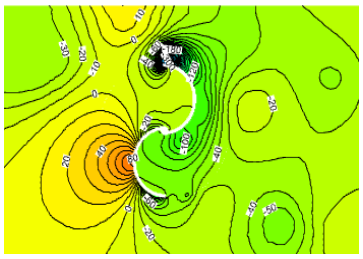	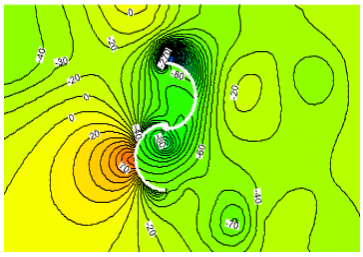
G/D = 2.0	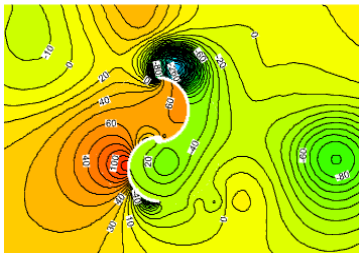	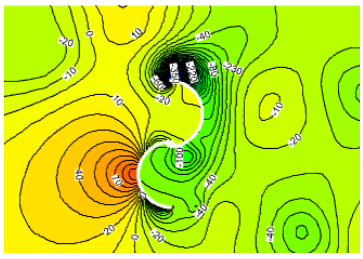	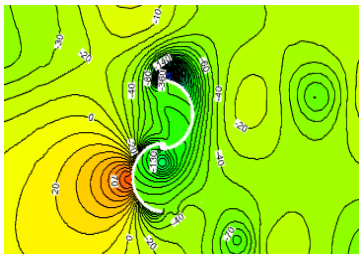
G/D = 2.25	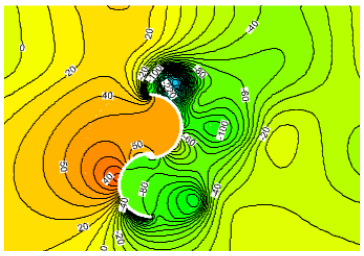	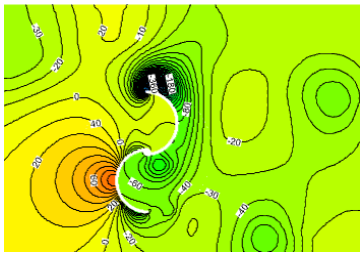	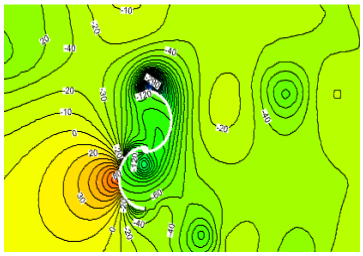

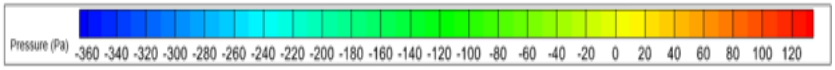

while the $\mathrm{G/D} = 2$ configuration exhibits negative values over the widest range ($\mathrm{TSR} \leq 0.8$). This indicates that wall placement also affects the performance of the rear turbine. As the gap increases, the influence of the deflected flow diminishes, and the rear turbine operates entirely within the wake region without the effect of the wall. Therefore, the optimal configuration for the rear turbine is $\mathrm{G/D} = 1.75$, which yields the highest moment and power coefficients compared to the other configurations. However, the rear turbine demonstrates good performance only at higher rotational speeds across all configurations. Hence, an optimal distance between the Savonius turbines is required to ensure effective operation even at low rotational speeds.

The velocity contour of the rear turbine (Table 7) indicates that it operates within a low wind velocity region. The relatively close spacing between the turbines causes the rear turbine to operate within the wake generated by the fore turbine. As the gap increases, a high-velocity flow develops at the tip of the advancing blade, indicating the presence of a nozzle effect within the gap. This nozzle effect contributes to the rear turbine rotating in the clockwise direction as the tip speed ratio increases.

At a tip speed ratio of 1.4, the increase in gap distance results in a wider vortex forming on the concave side of the returning blade. The expansion of this vortex has a negative impact, as it reduces the performance of the rear turbine. Consequently, the $\mathrm{G/D} = 2.25$ configuration exhibits lower performance compared to the other configurations.

The pressure contours of the rear turbine for all configurations are presented in Table 8. In the $\mathrm{G/D} = 2$ configuration at low tip speed ratios, a high-pressure region forms on the convex side of the returning blade, with a smaller high-pressure area observed on the concave side of the advancing blade. Additionally, a low-pressure region develops over a portion of the concave side of the advancing blade. This pressure distribution results in superior performance for the $\mathrm{G/D} = 2$ configuration compared to the others, with the turbine rotating in the counterclockwise direction at low tip speed ratios.

Across all configurations, as the tip speed ratio increases, a low-pressure region forms on the concave side of the advancing blade, causing the rear turbine to rotate

Table 7. Velocity contours of the fore turbine across all configurations at an azimuth angle of $90°$.

	Tip Speed Ratio		
	0.6	**1**	**1.4**
G/D = 1.75	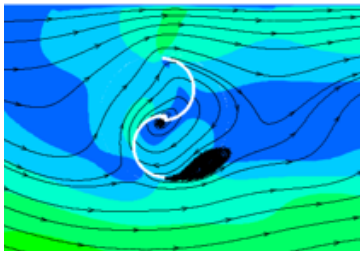	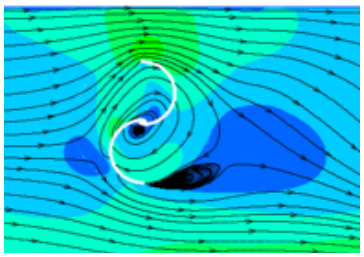	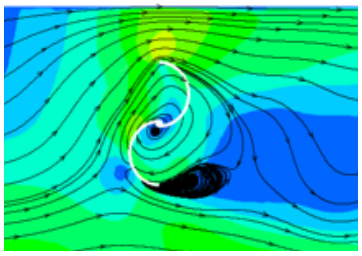
G/D = 2.0	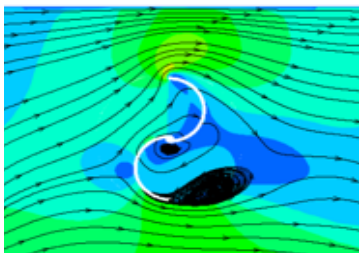	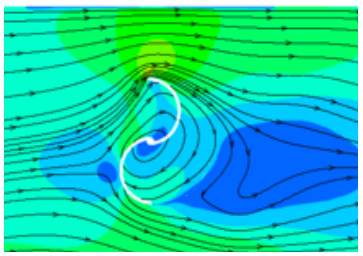	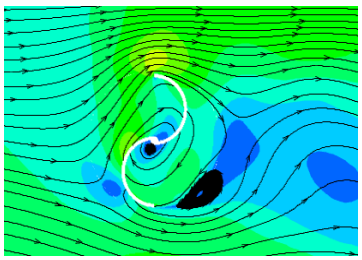
G/D = 2.25	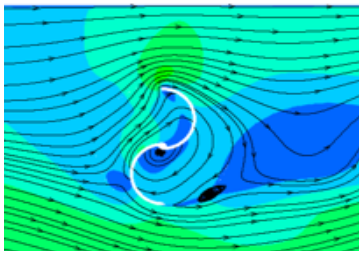	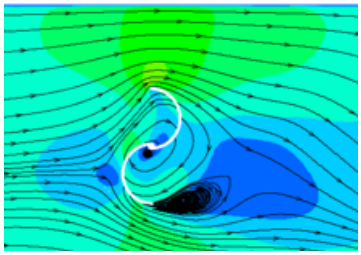	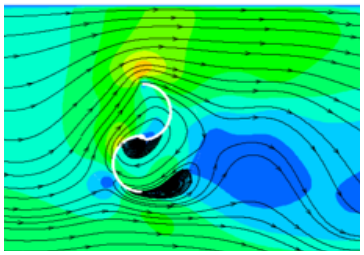

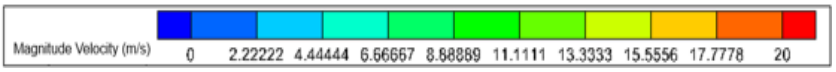

in the same direction as the incoming wind. Consequently, the larger pressure difference between the advancing and returning blades enhances the performance of the rear turbine. In particular, the $G/D = 1.75$ configuration demonstrates a consistently large pressure differential across all tip speed ratios, leading to improved performance compared to the other tandem configurations. This finding is particularly relevant for urban wind energy harvesting in Indonesia, where buildings in cities like Jakarta or Surabaya can act as flow concentrators. Integrating such turbines into building facades could overcome the challenges of low-speed urban winds.

4. Conclusions

This study investigates the effect of the distance between a Savonius turbine and a wall in a tandem configuration under a wind velocity of 7 m/s. The simulations were carried out using the Realizable k-epsilon turbulence model with enhanced wall treatment. Therefore, the results may not fully capture three-dimensional flow phenomena, transient turbulence structures, or real-world wind variability. Moreover, only three G/D ratios were examined, limiting the generalizability of the findings across a broader range of configurations. The presence of structural elements such as environmental turbulence and atmospheric boundary layer effects was not considered in this study. Future work should include experimental validation, three-dimensional simulations, and a wider variation of geometric parameters to strengthen the applicability of the results in practical installations. The conclusions drawn from this study are as follows:

1. The fore turbine in all configurations rotates in the counter-clockwise direction, which is attributed to the deflected flow caused by the presence of the wall.
2. The rear turbine rotates counter-clockwise at low tip speed ratios due to its operation within the wake region generated by the fore turbine. However, at higher tip speed ratios, the rear turbine tends to rotate clockwise up to its optimal tip speed ratio, as a result of the increasing blockage effect formed within the gap.
3. The rear turbine configuration, where the advancing blade is positioned adjacent to the wall, exhibits a

Table 8. Pressure contours of the fore turbine across all configurations at an azimuth angle of $90°$.

	Tip Speed Ratio		
	0.6	**1**	**1.4**
G/D = 1.75	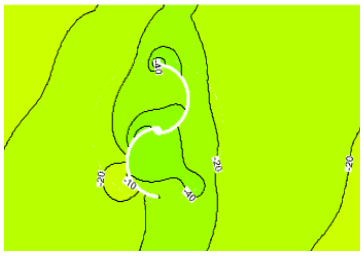	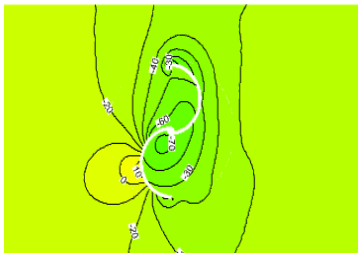	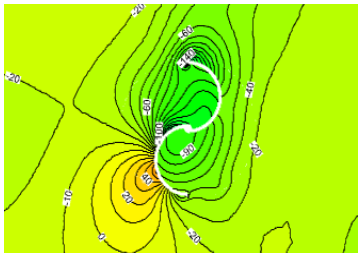
G/D = 2.0	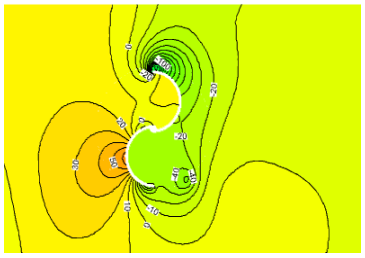	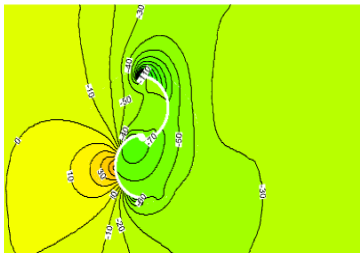	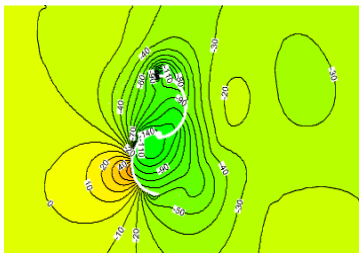
G/D = 2.25	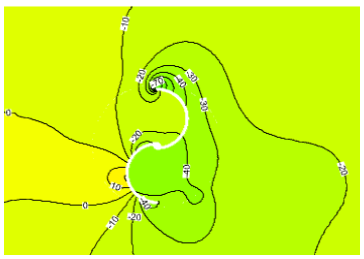	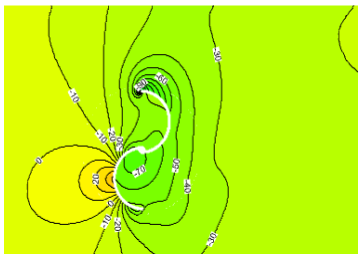	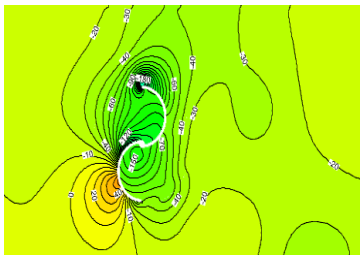
	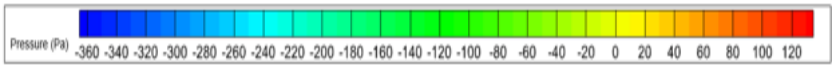		

negative impact across all configurations, as the maximum moment and power coefficients are achieved only at high tip speed ratios. Consequently, the rear turbine operates effectively only at high rotational speeds.

4. The $\mathrm{G/D} = 2$ configuration is identified as the optimal setup, as it produces the highest maximum moment and power coefficients compared to the other configurations. Furthermore, it demonstrates a relatively wide operating range of tip speed ratios, indicating that the Savonius turbine is capable of operating efficiently at high rotational speeds.

References

[1] S. G. of The National Energy Council, "Indonesia energy outlook 2024," 2024. Accessed: Jul. 24, 2025.

[2] P. D. Rosalina *et al.*, *Navigasi Isu Perubahan Iklim di Pemilu 2024: Panduan Komunikasi untuk Politisi*. Monash University, Indonesia: Monash Climate Change Communication Research Hub Indonesia Node, 2023. Accessed: Jul. 24, 2025.

[3] Pondera and Indonesian Institute for Energy Economics (IIEE), "Peta jalan pengembangan energi angin darat di indonesia," tech. rep., UNOPS Indonesia, Jakarta, 2023. Accessed: Jul. 24, 2025.

[4] A. K. Nag and S. Sarkar, "Performance analysis of helical savonius hydrokinetic turbines arranged in array," *Ocean Engineering*, vol. 241, 12 2021.

[5] Y. E. Priandika, T. Y. Yuwono, and R. Hermawan, "Numerical study of tandem installation of twin savonius hydrokinetic turbines on PLTU paiton cooling water channel," in *E3S Web of Conferences*, EDP Sciences, 4 2024.

[6] O. Wulaningtyas and T. Y. Yuwono, "Numerical study of the installation configuration of four savonius hydrokinetic turbines in the cooling water channel of PAITON power plant," 2025. [Online]. Available.

[7] M. Darvishyadegari and R. Hassanzadeh, "Evaluation of a savonius wind turbine in the vicinity of a circular cross-sectional building," *Journal of Building Engineering*, vol. 93, 9 2024.

[8] A. M. Abdelsalam, M. Abdelmordy, K. A. Ibrahim, and I. M. Sakr, "An investigation on flow behavior and performance of a wind turbine integrated within a building tunnel," *Energy*, vol. 280, 10 2023.

[9] X. Liu, D. Zhao, and N. L. Oo, "Numerical prediction of the power coefficient improvements of three laterally aligned savonius wind turbines above a forward facing step," *Journal of Wind Engineering and Industrial Aerodynamics*, vol. 228, 9 2022.

[10] P. A. Setiawan, T. Yuwono, and W. A. Widodo, "Numerical study of the stagger angle effect of a circular cylinder installed in front of returning blade toward the vertical axis savonius water turbine performance," in *Journal of Physics: Conference Series*, IOP Publishing, 8 2019.

[11] P. A. Setiawan, T. Yuwono, W. A. Widodo, E. Julianto, M. Santoso, and K. S. Surabaya, "Numerical study of a circular cylinder effect on the vertical axis savonius water turbine performance at the side of the advancing blade with horizontal distance variations," 2019.

[12] A. L. d. Santos *et al.*, "Development of a computational model for investigation of and oscillating water column device with a savonius turbine," 2022.

[13] S. A. Tomayahu, M. S. Rozaq, R. Romadhon, J. Pradipta, I. N. Haq, and E. Leksono, "Analisis pengaruh variasi laju aliran air pada sistem pendinginan modul fotovoltaik dengan simulasi CFD (computational fluid dynamics)," *Jurnal Otomasi Kontrol dan Instrumentasi*, vol. 16, no. 2, pp. 151–161, 2024.

[14] S. Roy and U. K. Saha, "Computational study to assess the influence of overlap ratio on static torque characteristics of a vertical axis wind turbine," in *Procedia Engineering*, pp. 694–702, Elsevier Ltd, 2013.

[15] M. H. Pranta, M. S. Rabbi, and M. M. Roshid, "A computational study on the aerodynamic performance of modified savonius wind turbine," *Results in Engineering*, vol. 10, 6 2021.

[16] M. Al-Ghriybah, M. F. Zulkafli, D. H. Didane, and S. Mohd, "Performance of the savonius wind rotor with two inner blades at low tip speed ratio," *CFD Letters*, vol. 12, no. 3, pp. 11–21, 2020.

[17] G. Sakti and T. Yuwono, "Numerical and experimental investigation of the effect of a circular cylinder as passive control on the savonius wind turbine performance," *Journal of Southwest Jiaotong University*, vol. 56, pp. 73–93, 12 2021.